ARCHIVE OF MECHANICAL ENGINEERING

DOI: 10.24425/ame.2025.154737 2025, Vol. 72, No. 2, pp. 271–292

Hassen ASSEM [1], Ahmed SAIMI [1], Ismail BENSAID [2], Abdelmadjid CHEIKH [2], Mouloud DAHMANE [3], Hassen AIT ATMANE [4]

Vibration and buckling analysis of quasi-3D porous composite steel-polymer concrete box section beams via DQFEM

Received 20 March 2025, **Revised** 7 June 2025, **Accepted** 16 June 2025, **Published online** 27 June 2025

Keywords: quasi 3D beam theory, free vibration, critical buckling, composite beam, porosity distribution

This paper presents a dynamic and critical buckling analysis of hollow steel box-section beams infilled with a porous polymer concrete composite core, modeled using a refined quasi-3D beam theory. The study investigates the effects of porosity in the polymer concrete core on the mechanical behavior of the beam. The governing equations are derived using the Differential Quadrature Finite Element Method (DQFEM) combined with Lagrange's principle. Results show that hollow steel-only beams exhibit the highest natural frequencies, while adding a composite core slightly reduces frequencies due to increased mass. Introducing porosity further lowers the frequencies, with a uniform porosity distribution (UDP) achieving better performance than non-uniform distributions. Increasing the slenderness ratio enhances natural frequencies across all configurations. For critical buckling loads, a solid (non-porous) core provides the highest capacity, while porosity reduces the load-bearing capacity compared to the solid core; however, UDP outperforms non-uniform distributions. Non-uniform porosity patterns demonstrate advantages in preserving structural integrity under certain conditions. The effects of slenderness ratio and boundary conditions are also

✉ Ahmed SAIMI, email: ahmed.saimi@univ-temouchent.edu.dz

[1]Mechanical Engineering Department, Faculty of Science and Technology, University Belhadj Bouchaib, Ain Temouchent, Algeria.

[2]IS2M Laboratory, Mechanical Engineering Department, Faculty of Technology, University Abou Beckr Beklaid, Tlemcen, Algeria.

[3]Department of Planning and Hydraulic Engineering, Higher National School of Hydraulics, Blida, Algeria.

[4]Department of Civil Engineering, Faculty of Civil Engineering and Architecture, University Hassiba Benbouali, Chlef, Algeria.

examined, highlighting their influence on dynamic and stability responses. The model is validated through comparisons with numerical and experimental results from the literature, demonstrating high accuracy. These findings provide valuable insights into the dynamic and buckling behavior of porous composite beams and offer practical guidelines for designing porous material-based structures in engineering applications.

1. Introduction

The study of composite beams has become increasingly significant due to their extensive applications in modern engineering structures, including bridges, aerospace systems, and machine tools [1]. Steel-polymer concrete beams, particularly those with porous cores, have emerged as a promising solution for improving structural performance due to their lightweight, high-energy dissipation, and tunable mechanical properties [2, 3]. The introduction of porosity into the concrete core offers additional advantages, such as reduced weight and enhanced energy absorption, but also adds complexity to their dynamic and stability behavior [4, 5]. Thus, accurately modeling and analyzing the effects of porosity have become a critical focus of research in structural mechanics [6, 7]. Advanced beam theories, such as the quasi-3D beam theory and higher-order deformation theories, have proven instrumental in capturing the effects of porosity and shear deformation behaviors in composite beams [8, 9]. Furthermore, these theories, when combined with numerical methods, allow for the detailed analysis of porous composite beams with various porosity distributions and slenderness ratios [10, 11].

The Differential Quadrature Finite Element Method (DQFEM) has been recognized as an efficient numerical tool for solving complex structural problems [12], including the vibration and stability analysis of porous and composite beams [13, 14]. This method, in combination with Lagrange's principle, has been successfully applied to derive governing equations for beams with porous and functionally graded materials [15, 16]. Additionally, experimental and numerical investigations have validated the effectiveness of these methods, highlighting their accuracy in predicting natural frequencies and buckling loads [17, 18].

Porous materials, particularly functionally graded porous cores, offer unique opportunities for tailoring material properties to meet specific design requirements [19–21]. However, the mechanical behavior of porous materials is highly dependent on the porosity distribution and structural dimensions, requiring detailed parametric studies to optimize their performance [6, 22, 23]. Recent research has also emphasized the importance of incorporating thermal and viscoelastic effects in the analysis of porous beams [24], further enhancing the accuracy of their dynamic and stability assessments [9, 25]. Composite beams are often reinforced with nanoparticles or graphene-based materials to enhance their dynamic and stability characteristics. Weijia et al. [26] investigated the dynamic response of sandwich beams with a functionally graded porous core subjected to pulse loads, demonstrating that porosity and graphene oxide powder significantly influence beam deflections.

Hung et al. [27] studied the analysis of free vibration in a sandwich beam featuring a porous functionally graded material (FGM) core under thermal conditions, employing a mesh-free methodology. Similarly, Assie et al. [28] explored the vibrational behavior of deep beams with viscoelastic cores, revealing that porosity and material damping play crucial roles in reducing dynamic amplitudes. Khafaji et al. [29] conducted a free vibration behavior study of sandwich beams, which consist of a porous functionally graded material (FGM) core sandwiched between two isotropic face layers, under the influence of thermal effects. The integration of nanoparticles in porous beams has also been a focus of research. Karegar et al. [30] examined the dynamic bending behavior of laminated porous concrete beams reinforced with nanoparticles, showing that increasing nanoparticle content can substantially reduce displacement. Stability studies have further contributed to understanding the mechanical behavior of FGP beams. Fortas et al. [31] analyzed buckling behavior using a finite element approach, emphasizing the impact of graphene reinforcement and porosity distributions on critical buckling loads. Additionally, Atmane et al. [32] studied FG beams on variable elastic foundations, highlighting the influence of porosity and gradient index on vibration responses.

Recent advances in the analysis of functionally graded materials (FGMs) have increasingly incorporated fractional calculus and nonlocal theories to capture scale-dependent behaviors in nano- and microscale structures. For instance, Arefi [33] developed nonlocal piezoelasticity relations for FG nanoplates under electric potential while accounting for thickness stretching effects. Rahimi [34] introduced a conformable fractional nonlocal model to study the nonlinear vibration of FGM nanobeams, highlighting the impact of fractional-order stress gradients. Chan [35] employed nonlocal strain gradient theory to analyze the buckling and vibration of FG sandwich cylindrical panels in thermal environments. Stempin [36] extended space-fractional beam models to Timoshenko formulations, validating their predictions experimentally. Additionally, Zenkour [37] investigated bending and buckling behaviors of FG plates on elastic foundations under hygrothermal conditions using advanced shear deformation theories.

These studies collectively enhance the understanding of porous FG structures for advanced applications. In this study, a refined quasi 3D beam theory is employed to model the dynamic and critical buckling behavior of porous steel-polymer concrete beams. The governing equations are derived using DQFEM and Lagrange's principle, considering the effects of porosity, slenderness ratios, and boundary conditions. Validation is performed by comparing the results with analytical, numerical, and experimental findings available in the literature, ensuring the reliability of the proposed approach. This research aims to provide valuable insights into the behavior of porous composite beams and contributes to the optimization of porous material-based structural systems for engineering applications.

The paper is organized as follows: the next section presents the theoretical formulation and models, including the steel-polymer porous concrete beam model, quasi-3D beam theory, and the DQFEM. The third section presents the numerical

results, analyzing the effects of beam porosity, slenderness, and boundary conditions on the dynamic behavior and stability. Finally, the conclusions and main results are summarized in the last section.

2. Formulation and theories

2.1. Porous steel-polymer concrete beam model

The concept of the steel-polymer concrete beam combines the synergistic properties of steel and polymer concrete to achieve enhanced mechanical performance, including stiffness, vibration energy dissipation, and dynamic adaptability. The beam structure includes a steel profile of length L with a square cross-section of $h \times b$ and e_s wall thickness, filled with polymer concrete (Fig.1). The polymer concrete core is composed of epoxy resin and mineral fillers of varying grain sizes, including ash, fine sand, medium gravel, and coarse gravel, ensuring optimized density and strength distribution [38]. By controlling the arrangement and degree of filling, the dynamic properties of such composite beams can be tailored to meet specific structural requirements.

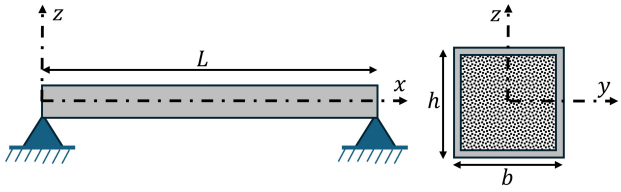

Fig. 1. Composite box beam model

The inclusion of porosity in the polymer concrete is explored to enhance the beam's lightweight and damping properties. The porosity distribution is modeled across the thickness of the beam using three distinct approaches: (a) Uniform Distribution of Porosity (UDP), (b) Symmetrical Non-Uniform Distribution of Porosity (NUDP1), and (c) Asymmetrical Non-Uniform Distribution of Porosity (NUDP2) (Fig. 2). In the UDP model, material properties such as Young's modulus

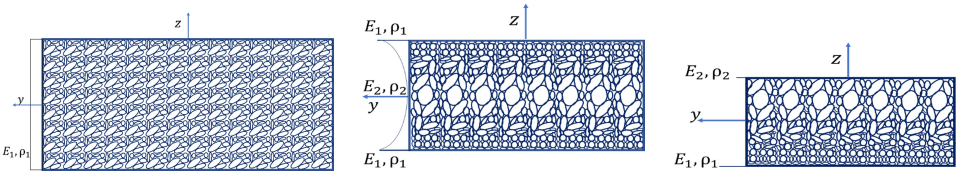

(a) (UDP) (b) (NUDP1) (c) (NUDP2)

Fig. 2. Porosity distributions patterns in the thickness direction: (a) Uniform distribution pattern (UDP), (b) non-uniform distribution pattern 1 (NUDP1), and (c) non-uniform distribution pattern 2 (NUDP2)

and density remain constant throughout the thickness. In the NUDP1 model, these properties peak at the extreme surfaces and decrease towards the mid-axis. In contrast, the NUDP2 model features maximum values at the lower surface, tapering off towards the upper surface. These distributions significantly influence the beam's mechanical and dynamic properties, including its natural frequencies and critical buckling loads.

The distribution of the properties of the material of the porous beam takes the form according to the following equations [19, 39]:

$$\text{UDP}: \begin{cases} E = E_1(1 - e_0\zeta), \\ \rho = \rho_1\sqrt{(1 - e_0\zeta)}, \end{cases} \tag{1}$$

$$\text{NUDP1}: \begin{cases} E\,(z) = E_1\left(1 - e_0\cos\left(\dfrac{\pi z}{(h - 2e_p)}\right)\right), \\ \rho(z) = \rho_1\left(1 - e_m\cos\left(\dfrac{\pi z}{(h - 2e_p)}\right)\right), \end{cases} \tag{2}$$

$$\text{NUDP2}: \begin{cases} E\,(z) = E_1\left(1 - e_0\cos\left(\dfrac{\pi z}{2(h - 2e_p)} + \dfrac{\pi}{4}\right)\right), \\ \rho(z) = \rho_1\left(1 - e_m\cos\left(\dfrac{\pi z}{2(h - 2e_p)} + \dfrac{\pi}{4}\right)\right), \end{cases} \tag{3}$$

with:

$$\begin{aligned} e_0 &= 1 - \frac{E_2}{E_1}, \quad 0 \leqslant e_0 < 1, \\ e_m &= 1 - \sqrt{(1 - e_0)}, \\ \zeta &= \frac{1}{e_0} - \frac{1}{e_0}\left(\frac{2}{\pi}\sqrt{1 - e_0} - \frac{2}{\pi} + 1\right)^2. \end{aligned} \tag{4}$$

Hence, ρ_1 and E_1 are minimum values of masse density and Young's modulus, respectively. E_2 and ρ_2 are maximum Young module values and density, respectively. e_0 and e_m are the porosity and mass porosity coefficients, respectively.

2.2. Quasi-3D beam model of a steel-polymer concrete beam

Based on the high order quasi-3D beam theory [6, 40], the displacement field at any arbitrary location on the beam is assumed to be stated as follows in the current work:

$$\begin{aligned} u_1(x, z, t) &= u(x, t) - z\frac{\mathrm{d}w_b(x, t)}{\mathrm{d}x} + f_1(z)\frac{\mathrm{d}w_s(x, t)}{\mathrm{d}x}, \\ u_3(x, z, t) &= w_b(x, t) + w_s(x, t) + f_2(z)w_z(x, t). \end{aligned} \tag{5}$$

This theory posits that the transverse displacement is categorized into three distinct components: w_b, w_s and w_z. Here, u represents the axial displacement along the x-axis, while w_b, w_s and w_z correspond to the bending, shear, and normal displacement components, respectively, of the transverse displacement for points situated along the beam's neutral axis.

The shear shape function $f_1(z)$ employed in this framework by equation (6) is derived from a third-order polynomial shear deformation beam theory, as established by [41] for both: equation (6) and $f_2(z) = 1 - f_1'(z)$. This function governs how the transverse shear strain is distributed along the thickness of the beam and captures the parabolic distribution of shear stresses through the beam thickness, eliminating the need for shear correction factors. Its formulation is critical to account for transverse shear deformation while satisfying physical and mathematical conditions with more realistic prediction of shear effects.

$$f_1(z) = \frac{4h}{5}\sinh\left(\frac{5z}{4h}\right) + z\left(-\cosh\left(\frac{5}{8}\right) + \frac{3}{20}\cos\left(\frac{5}{8}\right)\right). \tag{6}$$

The formula for strain energy, according to these theories, is as follows:

$$U = \frac{1}{2}\int_0^L \int_A \left(\sigma_{ij}\varepsilon_{ij}\right) \mathrm{d}A\,\mathrm{d}x. \tag{7}$$

Hence σ_{ij} and ε_{ij} represents the stress tensor and the strain tensor respectively which are defined by the following equations:

$$\begin{aligned}
\varepsilon_{xx} &= \frac{\mathrm{d}u}{\mathrm{d}x} = \frac{\mathrm{d}u}{\mathrm{d}x} - z\frac{\mathrm{d}^2 w_b}{\mathrm{d}x^2} - f_1\frac{\mathrm{d}^2 w_s}{\mathrm{d}x^2},\\
\varepsilon_{zz} &= \frac{\mathrm{d}w}{\mathrm{d}z} = \frac{\mathrm{d}f_2}{\mathrm{d}z}w_z,\\
\varepsilon_{xz} &= \frac{1}{2}\left(\frac{\mathrm{d}u}{\mathrm{d}z} + \frac{\mathrm{d}w}{\mathrm{d}x}\right) = \frac{1}{2}f_2\left(\frac{\mathrm{d}w_s}{\mathrm{d}x} + \frac{\mathrm{d}w_z}{\mathrm{d}x}\right),
\end{aligned} \tag{8}$$

$$\begin{aligned}
\sigma_{xx} &= (\lambda + 2\mu)\,\varepsilon_{xx} + \lambda\varepsilon_{zz},\\
\sigma_{xz} &= 2\mu\gamma_{xz},\\
\sigma_{zz} &= (\lambda + 2\mu)\,\varepsilon_{zz} + \lambda\varepsilon_{xx},
\end{aligned} \tag{9}$$

where:

$$\mu = \frac{E}{2(1+\nu)}, \tag{10}$$

$$\lambda = \frac{E\nu}{(1+\nu)(1-2\nu)}. \tag{11}$$

Hence μ and λ are the Lame constants, and ν is the Poisson's ratio. The substitution of equations (8)-(9) in equation (7) gives:

$$\begin{aligned} U = \frac{1}{2}\int_0^l \Bigg[& I_1\left(\frac{\mathrm{d}u}{\mathrm{d}x}\right)^2 - 2I_2\frac{\mathrm{d}u}{\mathrm{d}x}\frac{\mathrm{d}^2 w_b}{\mathrm{d}x^2} - 2I_3\frac{\mathrm{d}u}{\mathrm{d}x}\frac{\mathrm{d}^2 w_s}{\mathrm{d}x^2} \\ & + 2I_4\frac{\mathrm{d}^2 w_b}{\mathrm{d}x^2}\frac{\mathrm{d}^2 w_s}{\mathrm{d}x^2} + I_5\left(\frac{\mathrm{d}^2 w_b}{\mathrm{d}x^2}\right)^2 + I_6\left(\frac{\mathrm{d}^2 w_s}{\mathrm{d}x^2}\right)^2 \\ & + I_7 w_z^2 + 2I_8\frac{\mathrm{d}u}{\mathrm{d}x}w_z - 2I_9\frac{\mathrm{d}^2 w_b}{\mathrm{d}x^2}w_z \\ & - 2I_{10}\frac{\mathrm{d}^2 w_s}{\mathrm{d}x^2}w_z + I_{11}\left(\left(\frac{\mathrm{d}w_s}{\mathrm{d}x}\right)^2 + \left(\frac{\mathrm{d}w_z}{\mathrm{d}x}\right)^2 + 2\frac{\mathrm{d}w_s}{\mathrm{d}x}\frac{\mathrm{d}w_z}{\mathrm{d}x}\right)\Bigg]\mathrm{d}x, \end{aligned} \tag{12}$$

with:

$$\left\{I_{1,2,3,4,5,6,7}\right\} = \alpha_1\left(b\int_{-\frac{h}{2}}^{\frac{h}{2}} \mathbf{F}(z)\,\mathrm{d}z\right) + \beta_1\left((b-2e_s)\int_{-\frac{h}{2}+e_s}^{\frac{h}{2}-e_s} \mathbf{F}(z)\,\mathrm{d}z\right), \tag{13a}$$

$$\alpha_1 = \lambda_s + 2\mu_s, \tag{13b}$$

$$\beta_1 = (\lambda_c - \lambda_s) + 2(\mu_c - \mu_s), \tag{13c}$$

$$\mathbf{F}(z) = \left(1,\ z,\ f_1,\ zf_1,\ z^2,\ f_1^2,\ \left(\frac{\mathrm{d}f_2}{\mathrm{d}z}\right)^2\right), \tag{13d}$$

$$\left\{I_{8,9,10}\right\} = \alpha_2\left(b\int_{-\frac{h}{2}}^{\frac{h}{2}} \mathbf{G}(z)\,\mathrm{d}z\right) + \beta_2\left((b-2e_s)\int_{-\frac{h}{2}+e_s}^{\frac{h}{2}-e_s} \mathbf{G}(z)\,\mathrm{d}z\right), \tag{14a}$$

$$\alpha_2 = \lambda_s, \tag{14b}$$

$$\beta_2 = \lambda_c - \lambda_s, \tag{14c}$$

$$\mathbf{G}(z) = \frac{\mathrm{d}f_2}{\mathrm{d}z}\left(1,\ z,\ f_1\right), \tag{14d}$$

$$\{I_{11}\} = \mu_s\left(b\int_{-\frac{h}{2}}^{\frac{h}{2}} f_2^2\,\mathrm{d}z\right) + (\mu_c - \mu_s)\left((b-2e_s)\int_{-\frac{h}{2}+e_s}^{\frac{h}{2}-e_s} f_2^2\,\mathrm{d}z\right). \tag{15}$$

The kinetic energy can be written as:

$$T = \frac{1}{2}\int_0^l \left[J_1\left(\dot{u}^2 + \dot{w}_b^2 + \dot{w}_s^2 + 2\dot{w}_b\dot{w}_s\right) - 2J_2\dot{u}\frac{\mathrm{d}\dot{w}_b}{\mathrm{d}x} + 2J_3\dot{u}\frac{\mathrm{d}\dot{w}_s}{\mathrm{d}x} - 2J_4\frac{\mathrm{d}\dot{w}_b}{\mathrm{d}x}\frac{\mathrm{d}\dot{w}_s}{\mathrm{d}x} + J_5\left(\frac{\mathrm{d}\dot{w}_b}{\mathrm{d}x}\right)^2 + J_6\left(\frac{\mathrm{d}\dot{w}_s}{\mathrm{d}x}\right)^2 + J_7\dot{w}_z^2 + 2J_8\left(\dot{w}_b\dot{w}_z + \dot{w}_s\dot{w}_z\right)\right]\mathrm{d}x\,. \tag{16}$$

Hence the mass moments of inertia:

$$\left\{J_{1,2,3,4,5,6,7,8}\right\} = \alpha_3\left(b\int_{-\frac{h}{2}}^{\frac{h}{2}} \mathbf{H}(z)\,\mathrm{d}z\right) + \beta_3\left((b-2e_s)\int_{-\frac{h}{2}+e_s}^{\frac{h}{2}-e_s} \mathbf{H}(z)\,\mathrm{d}z\right), \tag{17a}$$

$$\alpha_3 = \rho_s, \tag{17b}$$

$$\beta_3 = \rho_c - \rho_s, \tag{17c}$$

$$\mathbf{H}(z) = \left(1,\ z,\ f_1,\ zf_1,\ z^2,\ f_1^2,\ f_2^2,\ f_2\right). \tag{17d}$$

With the subscripts s and c refer to for steel box and inner composite concrete, respectively.

The potential energy associated with the beam under an externally applied axial load is expressed as follows:

$$V = -\frac{1}{2}\int_0^L N_{cr}\left[\left(\frac{\mathrm{d}w_b}{\mathrm{d}x}\right)^2 + \left(\frac{\mathrm{d}w_s}{\mathrm{d}x}\right)^2 + 2\frac{\mathrm{d}w_b}{\mathrm{d}x}\frac{\mathrm{d}w_s}{\mathrm{d}x}\right]\mathrm{d}x. \tag{18}$$

2.3. DQFEM formulation

To represent our beam, we assume the shape functions take the form described in equation (19) [42]:

$$\begin{aligned} u\,[x] &= \sum_{i=1}^{N} L_i(x)\bar{u}_i, \\ w_b\,[x] &= \sum_{i=1}^{N} L_i(x)\bar{w}_{b_i}, \\ w_s\,[x] &= \sum_{i=1}^{N} L_i(x)\bar{w}_{s_i}, \\ w_z\,[x] &= \sum_{i=1}^{N} L_i(x)\bar{w}_{z_i}. \end{aligned} \tag{19}$$

This formulation employs L_i to denote the Lagrange polynomial, while $\bar{u}_i = u(x_i), \bar{w}_{b_i} = w_b(x_i), \bar{w}_{s_i} = w_s(x_i)$ and $\bar{w}_{z_i} = w_z(x_i)$ represent the nodal displacements at the Gauss-Lobatto quadrature points within the differential quadrature (DQ) finite element framework of the beam. The n-th order derivative of a field variable $f(x)$ at a discrete point x_i is approximated as follows:

$$\left.\frac{\partial^n f(x,t)}{\partial x^n}\right|_{x_i} = \sum_{j=1}^{N} A_{ij}^{(n)} f(x_j,t) \quad (i = 1,2,3,\ldots..,N)\,. \tag{20}$$

In this context, $A_{ij}^{(n)}$ denotes the weighting coefficient associated with the n-th order derivative approximation. $A_{ij}^{(n)}$ is derived as follows: if $n = 1$, so

$$\begin{aligned} A_{ij}^{(1)} &= \frac{M(x_i)}{(x_i - x_j)\,M(x_j)} \qquad i \neq j,\ i,j = 1,2,\ldots,N\,,\\ A_{ii}^{(1)} &= -\sum_{j=1,j\neq i}^{n} A_{ij}^{(1)} \qquad i = 1,2,\ldots,N\,, \end{aligned} \tag{21}$$

where:

$$M(x_i) = \prod_{k=1,k\neq i}^{N} (x_i - x_k)\,, \quad M(x_j) = \prod_{k=1,k\neq i}^{N} (x_j - x_k)\,. \tag{22}$$

The Gaussian-Lobatto quadrature rule with a degree of precision $(2n-3)$ for the function $f(x)$ defined in the interval $[-1,1]$ is:

$$\int_{-1}^{1} f(x)\,\mathrm{d}x = \sum_{j=1}^{N} C_j f(x_j), \tag{23}$$

$$\begin{aligned} C_1 = C_N &= \frac{2}{N(N-1)},\\ C_j &= \frac{2}{N(N-1)\left(P_{N-1}(x_j)\right)^2}\,, \quad (j \neq 1,N)\,. \end{aligned} \tag{24}$$

x_j corresponds to the $(j-1)$th root of the first derivative of the Legendre polynomial $P_{N-1}(x)$. To achieve fast convergence and high accuracy, a denser distribution of points near the boundaries is essential. Therefore, the sampling points are chosen based on the distribution of nodes in the Gauss–Lobatto grid and solved via Newton-Raphson iteration method:

$$x_j = -\cos\left(\frac{j-1}{N-1}\pi\right). \tag{25}$$

The relation between u and $\bar{u}$, w and $\bar{w}$ is defined using rule DQ [13]:

$$u = Q\bar{u}, \quad w_{b,s,z} = Q\bar{w}_{b,s,z}\,, \tag{26}$$

where

$$Q = \begin{bmatrix} 1 & 0 & 0 & \cdots & 0 & 0 \\ A^{(1)}_{1,1} & A^{(1)}_{1,2} & A^{(1)}_{1,3} & \cdots & A^{(1)}_{1,N-1} & A^{(1)}_{1,N} \\ 0 & 0 & 1 & \cdots & 0 & 0 \\ \vdots & \vdots & \vdots & \ddots & \vdots & \vdots \\ 0 & 0 & 0 & \cdots & 0 & 1 \\ A^{(1)}_{N,1} & A^{(1)}_{N,2} & A^{(1)}_{N,3} & \cdots & A^{(1)}_{N,N-1} & A^{(1)}_{N,N} \end{bmatrix}. \tag{27}$$

Utilizing the DQFEM, by substituting equations (19)-(27) into equations (12), (16), (18) and employing Lagrange's principle, we derive the subsequent system of equations.

$$\left[\begin{bmatrix} [K]_{11} & [K]_{12} & [K]_{13} & [K]_{14} \\ & [K]_{22} & [K]_{23} & [K]_{24} \\ & & [K]_{33} & [K]_{34} \\ \text{sym} & & & [K]_{44} \end{bmatrix} - \omega^2 \begin{bmatrix} [M]_{11} & [M]_{12} & [M]_{13} & [0] \\ & [M]_{22} & [M]_{23} & [M]_{24} \\ & & [M]_{33} & [M]_{34} \\ \text{sym} & & & [M]_{44} \end{bmatrix}\right] \begin{Bmatrix} u \\ w_b \\ w_s \\ w_z \end{Bmatrix} = \{0\}\,. \tag{28}$$

The mass matrix elements:

$$\begin{aligned} [M]_{11} &= \left[J_1 Q^T \bar{C}\, Q\right] \\ [M]_{12} &= -\left[J_2 Q^T \bar{C}\, \bar{A}^{(1)} Q\right] \\ [M]_{13} &= -\left[J_3 Q^T \bar{C}\, \bar{A}^{(1)} Q\right] \\ [M]_{22} &= \left[J_1 Q^T \bar{C} G_b + J_5 Q^T \bar{A}^{(1)^T} \bar{C} \bar{A}^{(1)} Q\right] \\ [M]_{23} &= \left[J_1 Q^T \bar{C} G_s + J_4 Q^T \bar{A}^{(1)^T} \bar{C} \bar{A}^{(1)} Q\right] \\ [M]_{24} &= \left[J_8 Q^T \bar{C} Q\right] \\ [M]_{33} &= \left[J_1 Q^T G_s + J_6 Q^T \bar{A}^{(1)^T} \bar{C} \bar{A}^{(1)} Q\right] \\ [M]_{34} &= \left[J_8 Q^T \bar{C} Q\right] \\ [M]_{44} &= \left[J_7 Q^T \bar{C} Q\right] \end{aligned} \tag{29}$$

The strain matrix elements:

$$
\begin{aligned}
[K]_{11} &= \left[I_1 Q^T \bar{A}^{(1)^T} \bar{C} \bar{A}^{(1)} Q\right] \\
[K]_{12} &= -\left[I_2 Q^T \bar{A}^{(1)^T} \bar{C} \bar{A}^{(2)} Q\right] \\
[K]_{13} &= -\left[I_3 Q^T \bar{A}^{(1)^T} \bar{C} \bar{A}^{(2)} Q\right] \\
[K]_{14} &= \left[I_8 Q^T \bar{A}^{(1)^T} \bar{C} Q\right] \\
[K]_{22} &= \left[I_5 Q^T \bar{A}^{(2)^T} \bar{C} \bar{A}^{(2)} Q\right] - N_{cr}\left[Q^T \bar{A}^{(1)^T} \bar{C} \bar{A}^{(1)} Q\right] \\
[K]_{23} &= \left[I_4 Q^T \bar{A}^{(2)^T} \bar{C} \bar{A}^{(2)} Q\right] - N_{cr}\left[Q^T \bar{A}^{(1)^T} \bar{C} \bar{A}^{(1)} Q\right] \\
[K]_{24} &= -\left[I_9 Q^T \bar{A}^{(2)^T} \bar{C} Q\right] \\
[K]_{33} &= \left[I_6 Q^T \bar{A}^{(2)^T} \bar{C} \bar{A}^{(2)} Q + I_{11} Q^T \bar{A}^{(1)^T} \bar{C} \bar{A}^{(1)} Q\right] - N_{cr}\left[Q^T \bar{A}^{(1)^T} \bar{C} \bar{A}^{(1)} Q\right] \\
[K]_{34} &= \left[I_{10} Q^T \bar{A}^{(2)^T} \bar{C} Q + I_{11} Q^T \bar{A}^{(1)^T} \bar{C} \bar{A}^{(1)} Q\right] \\
[K]_{44} &= \left[J_7 Q^T \bar{C} Q + I_{11} Q^T \bar{A}^{(1)^T} \bar{C} \bar{A}^{(1)} Q\right]
\end{aligned}
\tag{30}
$$

The interval $[-1, 1]$ is the only valid range for all kinds of node distributions in differentiation and quadrature. Therefore, the differential and quadrature matrices need to be adjusted as follows in order to put them into practice:

$$
\bar{C} = \frac{l_e}{2} C, \qquad \bar{A}^{(1)} = \frac{2}{l_e} A^{(1)}, \qquad \bar{A}^{(2)} = \frac{4}{{l_e}^2} A^{(2)}. \tag{31}
$$

l_e designate the beam element length.

3. Discussion of results

A beam with box shape section inner porous composite material and metal as outer material shown in Fig. 1 is studied in this section. The material properties for the outer material (steel): Young's modulus $E_{\text{steel}} = 210$ GPa, a mass density $\rho_{\text{steel}} = 7812$ Kg/m^3, Poisson's ratio $\nu_{\text{steel}} = 0.28$. The inner material used in this study is a composite polymer concrete [38]: Young's modulus $E_{\text{concrete}} = 17.2$ GPa, a mass density $\rho_{\text{concrete}} = 2200$ Kg/m^3, Poisson's ratio $\nu_{\text{concrete}} = 0.20$. In order to examine the current models, a comparative search is first carried out with the literature (Table 1), for a beam made from a steel profile measuring $L = 1000$ mm in length, featuring a square cross-section with dimensions of thickness $h = 70$ mm, and a width $b = 70$ mm and a wall thickness of $e_s = 3$ mm, which is internally filled with polymer concrete.

Table 1 show the natural frequencies of the composite beam predicted by the DQFEM-Q3D model closely match experimental results ($\leqslant 1.5\%$ deviation),

validating its accuracy. In contrast, classical beam theories show limitations: Timoshenko beam thoery (TBT) underestimates higher-mode frequencies (e.g., Mode 5: 3471 Hz vs. experimental 3589 Hz), while Euler Bernoulli beam theory (EBT) overestimates them significantly (e.g., Mode 5: 3957 Hz, 10.3% error). The literature's FEM model also overestimates higher modes (e.g., Mode 4: 2833 Hz vs. experimental 2572 Hz). These results confirm that the quasi-3D theory via DQFEM, which accounts for shear and material complexity, outperforms simplified models, making it ideal for dynamic analysis of composite beams.

Table 1. Natural frequencies (Hz) comparison with literatures

Mode shape	[38]		Present DQFEM		
	Experimental	FEM (TBT)	Q3D	TBT	EBT
1	339	338	340	337	352
2	899	915	905	880	962
3	1669	1755	1659	1618	1863
4	2572	2833	2595	2495	3027
5	3589	4124	3605	3471	3957

To facilitate ease of use in the parametric study, the nondimensional parameters outlined below are employed for all results presented in tables and figures. The frequency parameter ($\bar{\omega}$):

$$\bar{\omega} = \frac{\omega L^2}{h}\sqrt{\frac{\rho_s}{E_s}}, \tag{32}$$

The critical buckling load parameter ($\bar{N}_{cr}$):

$$\bar{N}_{cr} = \frac{12 N_{cr} L^2}{E_s b h^3}. \tag{33}$$

3.1. Free vibration analysis

The results presented in Table 2 and illustrated in Fig. 3 highlight the structural performance of clamped-clamped box-section beams with different core configurations, specifically focusing on frequencies. The steel box beam without a core shows the highest frequencies due to its rigid and homogeneous structure, while the addition of a solid core reduces the frequencies slightly because of the increased mass, despite the added stiffness. When porosity is introduced, the frequencies further decrease, with uniform porosity distribution (UDP) showing slightly better performance compared to non-uniform distributions (NUDP1 and NUDP2), where NUDP2 generally exhibits the lowest frequencies due to its less consistent stiffness distribution. As the aspect ratio (L/h) increases, the natural frequencies consistently rise across all configurations due to the geometric dependence of stiffness. Overall, while porous cores introduce weight savings, the choice of porosity pattern

significantly influences the mechanical performance, with uniform distributions offering the best balance between reduced weight and structural stability.

Table 2. Frequencies parameter of a clamped-clamped box-section beam with various composite polymer concrete core porosity patterns. $e_0 = 0.2$

L/h		Steel-only box beam	Solid core $e_0 = 0$	UPD	NUDP1	NUDP2
10	$\bar{\omega}_1$	7.9245	5.6643	5.7088	5.7309	5.714
	$\bar{\omega}_2$	20.1008	14.5787	14.6753	14.7247	14.6876
	$\bar{\omega}_3$	34.436	25.4698	25.5932	25.6606	24.8918
15	$\bar{\omega}_1$	8.3578	5.9077	5.9599	5.9854	5.9657
	$\bar{\omega}_2$	22.0465	15.7237	15.8514	15.9144	15.8661
	$\bar{\omega}_3$	39.9546	28.9075	29.1065	29.2072	29.1313
30	$\bar{\omega}_1$	8.6529	6.0675	6.1253	6.1533	6.1316
	$\bar{\omega}_2$	23.5565	16.5648	16.7189	16.7938	16.7357
	$\bar{\omega}_3$	45.0679	31.8608	32.1434	32.2815	32.1748

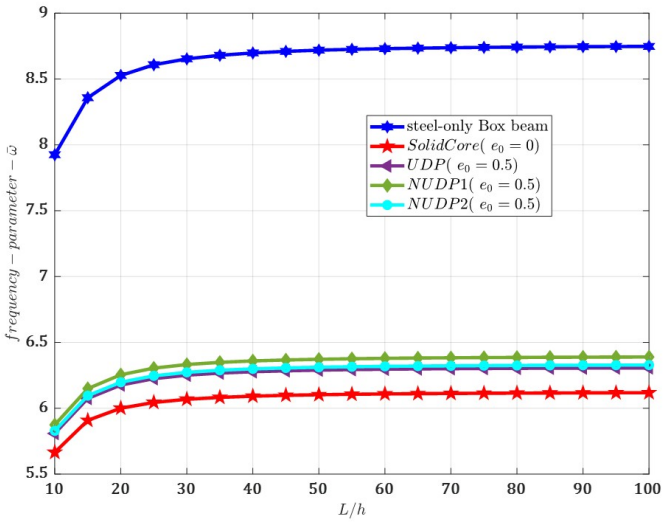

Fig. 3. Frequency parameters $\bar{\omega}_1$ according to length/thickness ratio for various porosity distributions ($e_0 = 0.5$)

The results in Table 3, supported by Fig. 4, highlight the relationship between porosity index (e_0), porosity distribution patterns (UDP, NUDP1, NUDP2), and boundary conditions on the dynamic performance of a steel box-section beam with a composite polymer concrete core. These results provide critical insights into the behavior of the structure under various configurations.

As shown in Table 3 and Fig. 4, the frequency parameters slightly increase with the porosity index (e_0) across all boundary conditions. This trend is consistent

Table 3. Frequencies parameters of box-section beam with various core porosity patterns and boundary conditions $L/h = 15$

e_0	NNF								
	UPD			NUDP1			NUDP2		
	$\bar{\omega}_1$	$\bar{\omega}_2$	$\bar{\omega}_3$	$\bar{\omega}_1$	$\bar{\omega}_2$	$\bar{\omega}_3$	$\bar{\omega}_1$	$\bar{\omega}_2$	$\bar{\omega}_3$
	Simply supported beam								
0	2.673	10.409	22.477	2.673	10.409	22.477	2.673	10.409	22.477
0.2	2.699	10.503	22.661	2.711	10.548	22.751	2.702	10.513	22.682
0.4	2.733	10.627	22.909	2.760	10.727	23.107	2.740	10.653	22.963
0.6	2.780	10.804	23.264	2.826	10.972	23.602	2.795	10.855	23.375
0.8	2.857	11.090	23.845	2.928	11.355	24.385	2.885	11.187	24.066
steel-only	3.813	14.733	31.489	3.813	14.733	31.489	3.813	14.733	31.489
	Clamped-clamped beam								
0	5.907	15.723	28.907	5.907	15.723	28.907	5.907	15.723	28.9075
0.2	5.959	15.851	29.106	5.985	15.914	29.207	5.965	15.866	29.131
0.4	6.029	16.023	29.381	6.085	16.163	29.607	6.044	16.061	29.449
0.6	6.128	16.271	29.785	6.224	16.508	30.176	6.157	16.348	29.929
0.8	6.289	16.676	30.460	6.440	17.057	31.106	6.345	16.830	30.760
steel-only	8.357	22.046	39.954	8.357	22.046	39.954	8.357	22.046	39.954
	Clamped-free beam								
0	0.958	5.853	15.770	0.958	5.853	15.770	0.958	5.853	15.770
0.2	0.967	5.906	15.901	0.972	5.932	15.964	0.968	5.912	15.915
0.4	0.980	5.977	16.077	0.989	6.033	16.217	0.982	5.991	16.115
0.6	0.997	6.077	16.32	1.013	6.172	16.567	1.002	6.106	16.406
0.8	1.025	6.239	16.739	1.050	6.389	17.120	1.033	6.294	16.892
steel-only	1.368	8.292	22.111	1.368	8.292	22.111	1.368	8.292	22.111

for all porosity patterns (UDP, NUDP1, NUDP2). The slight increase is due to the dominance of the reduction in core mass over the reduction in stiffness, leading to an improvement in the stiffness-to-mass ratio. This effect is particularly evident in clamped-clamped beams (Fig. 4a), which exhibit the highest frequency values compared to simply supported (Fig. 4b) and clamped-free beams (Fig. 4c). This outcome reflects the ability of fully fixed boundary conditions to enhance the overall rigidity of the beam, amplifying the dynamic response. Among the porosity patterns, NUDP1 consistently yields the highest frequency parameters across all boundary conditions. This indicates that a strategically non-uniform distribution of porosity enhances stiffness retention while reducing mass effectively. In comparison, UDP shows the lowest frequency values due to its uniform distribution, which does not optimize the stiffness-to-mass ratio as efficiently. The steel-only box beam demonstrates significantly higher frequency parameters compared to the composite beams. However, the difference narrows as (e_0) increases, indicating that at higher porosity levels, the reduction in core density diminishes the impact

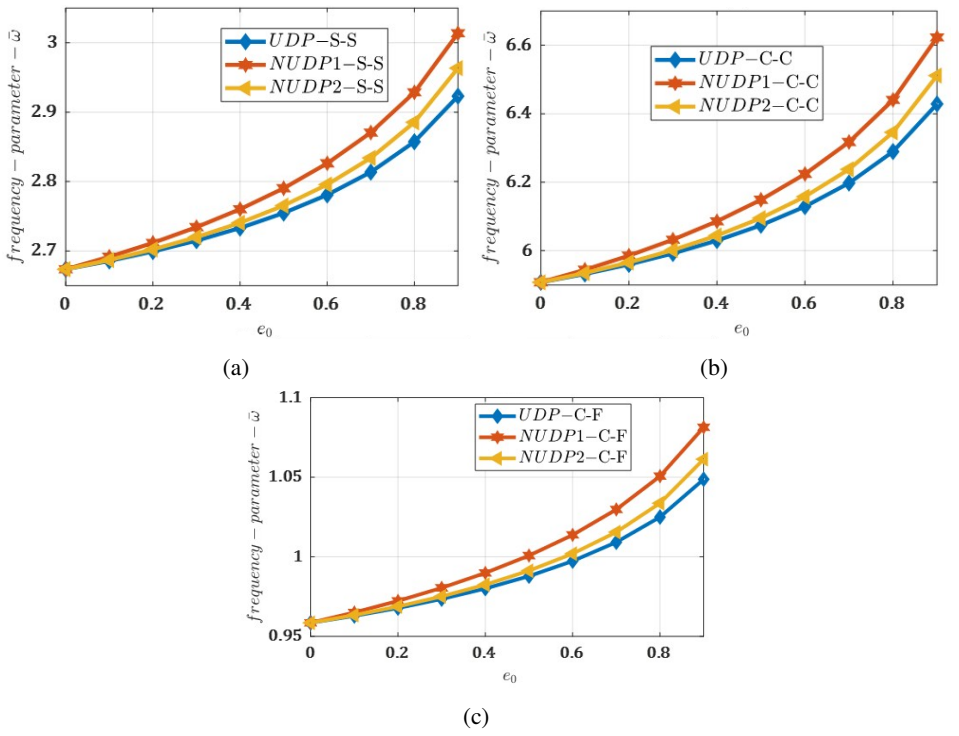

Fig. 4. Frequency parameters $\bar{\omega}_1$ for various porosity distributions based on porosity coefficient ($L/h = 15$), (a): clamped-clamped, (b): simply supported-simply supported, (c): clamped-free

of the composite material on dynamic behavior. This suggests that for lightweight applications requiring higher frequencies, optimizing the porosity distribution is essential.

3.2. Buckling analysis

The results presented in Table 4 and illustrated in Fig. 5 highlight the structural performance of clamped-clamped box-section beams with different core configurations, specifically focusing on critical buckling loads. Regarding critical buckling loads, the steel-only beam performs the worst, while the addition of a solid core significantly enhances the load-bearing capacity, demonstrating the core's contribution to resisting buckling. The introduction of porosity reduces the critical buckling loads compared to the solid core but still outperforms the steel-only configuration. UDP generally provides higher buckling loads than NUDP1 and NUDP2, confirming that a uniform porosity distribution maintains better structural integrity. The effect of increasing the aspect ratio is also notable for buckling loads, as all configurations see substantial improvements in their critical loads with larger L/h values.

Table 4. Critical buckling parameter of a clamped-clamped box-section beam with porous composite polymer concrete core and steel outer layer. $e_0 = 0.2$

L/h		Steel-only box beam	Solid core $e_0 = 0$	UPD	NUDP1	NUDP2
10	$\bar{N}_{cr1}$	2.2112	3.0279	2.9367	2.9528	2.9408
	$\bar{N}_{cr2}$	2.2164	3.0300	2.9368	2.9528	2.9409
	$\bar{N}_{cr3}$	2.2302	3.0554	2.9612	2.9774	2.9654
15	$\bar{N}_{cr1}$	5.3810	7.3613	7.1312	7.1703	7.1412
	$\bar{N}_{cr2}$	5.4086	7.3725	7.1478	7.1873	7.1580
	$\bar{N}_{cr3}$	5.6170	7.4762	7.2642	7.3049	7.2745
30	$\bar{N}_{cr1}$	11.8146	14.1205	13.8224	13.9498	13.8506
	$\bar{N}_{cr2}$	23.9438	28.7424	28.1251	28.3793	28.1817
	$\bar{N}_{cr3}$	31.1480	41.0561	40.1257	40.3641	40.1850

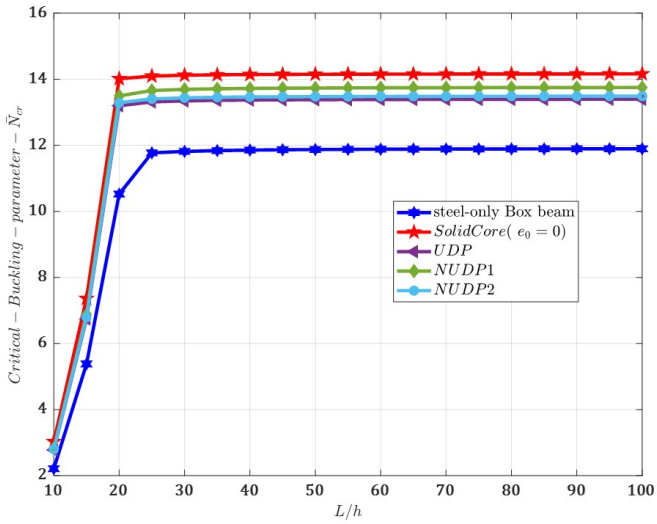

Fig. 5. Critical Buckling parameters $\bar{N}_{cr1}$ according to length/thickness ratio for various porosity distributions ($e_0 = 0.5$)

The results in Table 5, supported by Fig. 6, highlight the relationship between porosity index (e_0), porosity distribution patterns (UDP, NUDP1, NUDP2), and boundary conditions on the stability performance of a steel box-section beam with a composite polymer concrete core. The critical buckling parameters in Table 5 and Fig. 6 show a contrasting trend compared to frequency parameters. As (e_0) increases, the critical buckling loads decrease significantly across all boundary conditions and porosity patterns. This behavior reflects the substantial reduction in stiffness caused by increased porosity, which compromises the beam's ability to resist compressive loads. The reduction is most pronounced in clamped-free beams (Fig. 6c), where the lack of support at one end further amplifies the effect of stiffness loss. Clamped-clamped beams (Fig. 6a) exhibit the highest critical

Table 5. Critical buckling parameters of box-section beam with various core porosity patterns and boundary conditions $L/h = 15$

e_0	NNF								
	UPD			NUDP1			NUDP2		
	$\bar{N}_{cr1}$	$\bar{N}_{cr2}$	$\bar{N}_{cr3}$	$\bar{N}_{cr1}$	$\bar{N}_{cr2}$	$\bar{N}_{cr3}$	$\bar{N}_{cr1}$	$\bar{N}_{cr2}$	$\bar{N}_{cr3}$
	Simply supported beam								
0	3.527	6.773	6.785	3.527	6.773	6.785	3.527	6.773	6.785
0.2	3.453	6.564	6.574	3.485	6.600	6.610	3.460	6.573	6.583
0.4	3.375	6.337	6.346	3.442	6.422	6.431	3.393	6.365	6.374
0.6	3.290	6.085	6.092	3.399	6.239	6.246	3.326	6.147	6.154
0.8	3.194	5.786	5.789	3.356	6.051	6.056	3.258	5.919	5.923
steel-only	2.952	4.940	4.951	2.952	4.940	4.951	2.952	4.940	4.951
	Clamped-clamped beam								
0	7.361	7.373	7.476	7.361	7.373	7.476	7.361	7.373	7.476
0.2	7.131	7.148	7.264	7.170	7.187	7.305	7.141	7.158	7.275
0.4	6.882	6.903	7.035	6.974	6.996	7.129	6.912	6.934	7.065
0.6	6.604	6.630	6.780	6.773	6.799	6.949	6.673	6.698	6.847
0.8	6.276	6.306	6.477	6.567	6.596	6.763	6.422	6.451	6.617
steel-only	5.381	5.409	5.617	5.381	5.409	5.617	5.381	5.409	5.617
	Clamped-free beam								
0	0.880	3.377	7.207	0.880	3.377	7.207	0.880	3.377	7.207
0.2	0.861	3.265	6.999	0.869	3.285	7.038	0.863	3.270	7.009
0.4	0.842	3.143	6.774	0.859	3.190	6.866	0.846	3.158	6.803
0.6	0.821	3.006	6.524	0.848	3.092	6.688	0.829	3.040	6.588
0.8	0.797	2.843	6.228	0.838	2.990	6.506	0.811	2.915	6.363
steel-only	0.738	2.382	5.378	0.738	2.382	5.378	0.738	2.382	5.378

buckling loads, showcasing their superior stability due to the increased constraints. Simply supported beams (Fig. 6b) show intermediate buckling performance, while clamped-free beams consistently display the lowest resistance to buckling, making them the most sensitive to porosity-related stiffness loss. Among the porosity patterns, NUDP1 again demonstrates superior performance, maintaining higher critical buckling loads compared to UDP and NUDP2 at all (e_0) levels. This highlights the advantage of non-uniform porosity distributions in mitigating the adverse effects of stiffness reduction by strategically reinforcing critical regions of the beam. The steel-only box beam exhibits lower critical buckling loads compared to composite beams at all porosity levels. This outcome underscores the effectiveness of the polymer concrete core in distributing compressive stresses, even as porosity increases. The composite structure's ability to outperform the steel-only beam in stability applications demonstrates the value of combining lightweight core materials with optimized porosity for enhanced structural integrity.

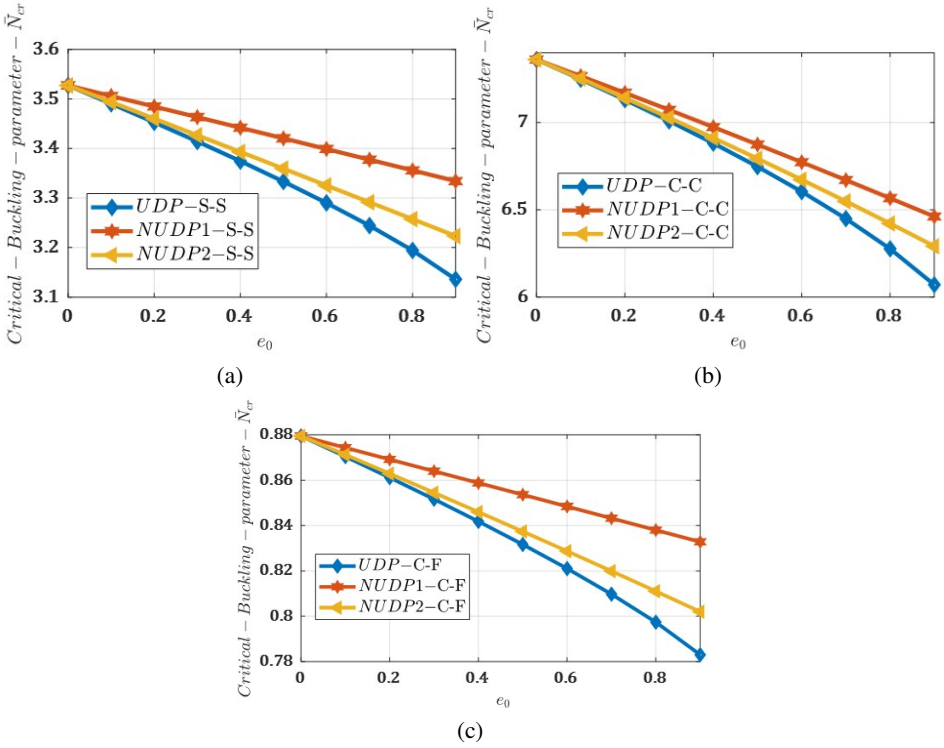

Fig. 6. Critical Buckling parameters $\bar{N}_{cr1}$ for various porosity distributions based on porosity coefficient ($L/h = 15$), (a): clamped-clamped, (b): simply supported-simply supported, (c): clamped-free

4. Conclusions

This study provides a comprehensive analysis of the vibration and buckling performance of porous composite steel-polymer concrete box-section beams using a refined quasi-3D beam theory combined with the Differential Quadrature Finite Element Method (DQFEM). The investigation highlights the influence of porosity index, porosity distribution patterns, and boundary conditions on the structural performance, offering valuable insights for the design of lightweight, efficient, and stable structures. The key findings are summarized as follows:

- The introduction of porosity in the polymer concrete core slightly increases the frequencies parameters $\bar{\omega}$ due to the dominant effect of reduced mass over reduced stiffness, enhancing the stiffness-to-mass ratio.
- Clamped-clamped beams exhibit the highest natural frequencies across all configurations, demonstrating the beneficial impact of fully constrained boundary conditions on the dynamic response.
- Among porosity distribution patterns, NUDP1 consistently demonstrates the highest frequency parameters and critical buckling loads, highlighting that

strategically non-uniform porosity not only enhances stiffness retention and dynamic performance but also mitigates stiffness reduction while improving load-bearing capacity more effectively than UDP or NUDP2.

- Steel-only box beams achieve higher frequency values than composite beams due to their rigid and homogeneous structure. However, as the porosity index increases, the difference in frequency values narrows, underscoring the potential of porous composite beams for lightweight applications.
- Critical buckling loads $\bar{N}_{cr}$ decrease significantly with increasing porosity index due to the associated reduction in stiffness, which compromises the beam's resistance to compressive loads.
- Clamped-clamped beams achieve the highest buckling loads due to their superior stability, while clamped-free beams display the lowest resistance to buckling, making them most sensitive to stiffness loss caused by porosity.
- Composite beams with a porous polymer concrete core outperform steel-only beams in critical buckling loads across all configurations, emphasizing the value of combining lightweight core materials with optimized porosity distributions to enhance stability.
- Increasing the slenderness ratio consistently improves both natural frequencies and critical buckling loads for all porosity configurations and boundary conditions, demonstrating the geometric influence on the beam's stiffness and stability.
- The results highlight that while porous polymer concrete cores reduce the overall weight of the structure, careful optimization of porosity distribution is critical to maintaining or enhancing structural performance.
- Uniform porosity distributions (UDP) provide a balance between dynamic and stability performance, while non-uniform patterns (NUDP1) offer superior stiffness and load-bearing capacity, making them more suitable for high-performance engineering applications.

In conclusion, this study demonstrates the feasibility of using porous composite steel-polymer concrete beams for lightweight and stable structural applications. By leveraging advanced modeling techniques such as quasi-3D beam theory and DQFEM, and optimizing porosity distribution patterns, engineers can design efficient structures that balance dynamic performance, weight reduction, and stability. These findings offer practical guidelines for implementing porous material-based designs in aerospace, automotive, and civil engineering fields.

However, some limitations should be acknowledged. The analysis assumes ideal material behavior without accounting for potential imperfections, damage, or long-term degradation in real-world conditions. Additionally, thermal effects, moisture ingress, and manufacturing-induced variability were not considered in the current modeling framework. Experimental validation was beyond the scope of this study, and the numerical results would benefit from corroboration through laboratory testing.

Future research could extend this work by incorporating thermo-mechanical coupling, investigating fatigue and durability under cyclic loading, and exploring more complex geometries and loading conditions. Moreover, optimization studies integrating multi-objective design criteria could further enhance the practical applicability of porous composite beams in advanced engineering structures.

References

[1] S.-Ch. Han, I. Kreja, G. Rus, and G.R. Lomboy. Structural dynamics and stability of composite structures. *Advances in Materials Science and Engineering*, 2016(1):7468181, 2016. doi: 10.1155/2016/7468181.

[2] S. Berczyński and T. Wróblewski. Vibration of steel–concrete composite beams using the timoshenko beam model. *Journal of Vibration and Control*, 11(6):829–848, 2005. doi: 10.1177/1077546305054678.

[3] P. Dunaj, S. Berczyński, M. Chodźko, and B. Niesterowicz. Finite element modeling of the dynamic properties of composite steel–polymer concrete beams. *Materials*, 13(7):1630, 2020. doi: 10.3390/ma1630.

[4] M.R. Barati and A.M. Zenkour. Investigating post-buckling of geometrically imperfect metal foam nanobeams with symmetric and asymmetric porosity distributions. *Composite Structures*, 182:91–98, 2017. doi: 10.1016/j.compstruct.2017.09.008.

[5] D. Chen, J. Yang, and S. Kitipornchai. Elastic buckling and static bending of shear deformable functionally graded porous beam. *Composite Structures*, 133:54–61. doi: 10.1016/j.compstruct.2015.07.052.

[6] I. Bensaid, A. Saimi, and Ö. Civalek. Effect of two-dimensional material distribution on dynamic and buckling responses of graded ceramic-metal higher order beams with stretch effect. *Mechanics of Advanced Materials and Structures*, pages 1–17, 2022. doi: 10.1080/15376494.2022.2142342.

[7] Y.Q. Wang, H.L. Zhao, Ch. Ye, and J.W. Zu. A porous microbeam model for bending and vibration analysis based on the sinusoidal beam theory and modified strain gradient theory. *International Journal of Applied Mechanics*, 10(05):1850059, 2018. doi: 10.1142/s175882511850059x.

[8] M. Avcar, L. Hadji, and Ö. Civalek. Natural frequency analysis of sigmoid functionally graded sandwich beams in the framework of high order shear deformation theory. *Composite Structures*, 276:114564, 2021. doi: 10.1016/j.compstruct.2021.114564.

[9] A. Saimi, I. Bensaid, and A. Fellah. Effect of crack presence on the dynamic and buckling responses of bidirectional functionally graded beams based on quasi-3d beam model and differential quadrature finite element method. *Archive of Applied Mechanics*, 2023. doi: 10.1007/s00419-023-02429-w.

[10] F. Ebrahimi and A. Jafari. A four-variable refined shear-deformation beam theory for thermo-mechanical vibration analysis of temperature-dependent fgm beams with porosities. *Mechanics of Advanced Materials and Structures*, 25(3):212–224, 2018. doi: 10.1080/15376494.2016.1255820.

[11] S. Thai, H.T. Thai, T.P. Vo, and V.I. Patel. Size-dependant behaviour of functionally graded microplates based on the modified strain gradient elasticity theory and isogeometric analysis. *Computers & Structures*, 190:219–241, 2017. doi: 10.1016/j.compstruc.2017.05.014.

[12] I.E. Houalef, I. Bensaid, A. Saimi, and A. Cheikh. An analysis of vibration and buckling behaviors of nano-composite beams reinforced with agglomerated carbon nanotubes via differential quadrature finite element method. *Mechanics of Advanced Materials and Structures*, pages 1–19, 2023. doi: 10.1080/15376494.2023.2185706.

[13] A. Saimi, A. Hadjoui andI. Bensaid, and A. Fellah. An differential quadrature finite element and the differential quadrature hierarchical finite element methods for the dynamics analysis of on board shaft. *European Journal of Computational Mechanics*, 29(4-6):303–344, 2021. doi: 10.13052/ejcm1779-7179.29461.

[14] C. Liu, B. Liu, L. Zhao, Y. Xing, Ch. Ma, and H. Li. A differential quadrature hierarchical finite element method and its applications to vibration and bending of mindlin plates with curvilinear domains. *International Journal for Numerical Methods in Engineering*, 109(2):174–197, 2017. doi: 10.1002/nme.5277.

[15] D. Chen, S. Kitipornchai, and J. Yang. Nonlinear free vibration of shear deformable sandwich beam with a functionally graded porous core. *Thin-Walled Structures*, 107:39–48, 2016. doi: 10.1016/j.tws.2016.05.025.

[16] M. Jabbari, A. Mojahedin, A. R. Khorshidvand, and M.R. Eslami. Buckling analysis of a functionally graded thin circular plate made of saturated porous materials. *Journal of Engineering Mechanics*, 140(2):287–295, 2014. doi: doi:10.1061/(ASCE)EM.1943-7889.0000663.

[17] B. Peeters, H. Van der Auweraer, P. Guillaume, and J. Leuridan. The polymax frequency-domain method: A new standard for modal parameter estimation? *Shock and Vibration*, 11(3-4):523692, 2004. doi: 10.1155/2004/523692.

[18] R. Xu and Y.-F. Wu. Free vibration and buckling of composite beams with interlayer slip by two-dimensional theory. *Journal of Sound and Vibration*, 313(3):875–890, 2008. doi: 10.1016/j.jsv.2007.12.029.

[19] I. Bensaid and A. Saimi. Dynamic investigation of functionally graded porous beams resting on viscoelastic foundation using generalised differential quadrature method. *Australian Journal of Mechanical Engineering*, pages 1–20, 2022. doi: 10.1080/14484846.2021.2017115.

[20] M. Dahmane, M. Benadouda, A. Fellah, A. Saimi, A.A. Hassen, and I. Bensaid. Porosities-dependent wave propagation in bi-directional functionally graded cantilever beam with higher-order shear model. *Mechanics of Advanced Materials and Structures*, pages 1–11. doi: 10.1080/15376494.2023.2253546.

[21] N. Wattanasakulpong and V. Ungbhakorn. Linear and nonlinear vibration analysis of elastically restrained ends fgm beams with porosities. *Aerospace Science and Technology*, 32(1):111–120, 2014. doi: 10.1016/j.ast.2013.12.002.

[22] L. Ke, Y. Wang, and Z. Wang. Thermal effect on free vibration and buckling of size-dependent microbeams. *Physica E: Low-dimensional Systems and Nanostructures*, 43(7):1387–1393, 2011. doi: 10.1016/j.physe.2011.03.009.

[23] P.T. Thang, T. Nguyen-Thoi, D. Lee, J. Kang, and J. Lee. Elastic buckling and free vibration analyses of porous-cellular plates with uniform and non-uniform porosity distributions. *Aerospace Science and Technology*, 79:278–287, 2018. doi: 10.1016/j.ast.2018.06.010.

[24] V. Mahesh. Porosity effect on the nonlinear deflection of functionally graded magneto-electro-elastic smart shells under combined loading. *Mechanics of Advanced Materials and Structures*, 29(19):2707–2725, 2022. doi: 10.1080/15376494.2021.1875086.

[25] Z. Huang, X. Wang, N. Wu, F. Chu, and J. Luo. A finite element model for the vibration analysis of sandwich beam with frequency-dependent viscoelastic material core. *Materials*, 12(20):3390, 2019. doi: 10.3390/ma12203390.

[26] W. Yu and L. Zhou. Dynamic/static stability characteristics of sandwich fg porous beams. *Steel and Composite Structures*, 46(2):203–210, 2023. doi: 10.12989/SCS.2023.46.2.203.

[27] T.Q. Hung, T.M. Tu, and D.M. Duc. Free vibration analysis of sandwich beam with porous fgm core in thermal environment using mesh-free approach. *Archive of Mechanical Engineering*, 69(3):471–496, 2022. doi: 10.24425/ame.2022.140422.

[28] A. Assie, S.D. Akbas, A.M. Kabeel, A.A. Abdelrahman, and M.A. Eltaher. Dynamic analysis of porous functionally graded layered deep beams with viscoelastic core. *Steel and Composite Structures*, 43(1):79–90, 2022. doi: 10.12989/SCS.2022.43.1.079.

[29] S.O.W. Khafaji, M.A. Al-Shujairi, and M.J. Aubad. Transient analysis of transversely functionally graded timoshenko beam (tfgtb) in conjunction with finite element method. *Archive of Mechanical Engineering*, vol. 67(No 3):299–321, 2020. doi: 10.24425/ame.2020.131694.

[30] M. Karegar, M.R. Bidgoli, and H. Mazaheri. Dynamic bending analysis of laminated porous concrete beam reinforced by nanoparticles considering porosity effects. *Steel and Composite Structures*, 43(1):129–137, 2022. doi: 10.12989/SCS.2022.43.1.129.

[31] L. Fortas, A. Messai, T. Merzouki, and M.S.A. Houari. Elastic stability of functionally graded graphene reinforced porous nanocomposite beams using two variables shear deformation. *Steel and Composite Structures*, 43(1):31–54, 2022. doi: 10.12989/SCS.2022.43.1.031.

[32] R.A. Atmane, N. Mahmoudi, R. Bennai, H.A. Atmane, and A. Tounsi. Investigation on the dynamic response of porous fgm beams resting on variable foundation using a new higher order shear deformation theory. *Steel and Composite Structures*, 39(1):95–107, 2021. doi: 10.12989/SCS.2021.39.1.095.

[33] M. Arefi and A.H.S. Arani. Nonlocal vibration analysis of the three-layered fg nanoplates subjected to applied electric potential considering thickness stretching effect. *Proceedings of the Institution of Mechanical Engineers, Part L*, 234(9):1183–1202, 2020. doi: 10.1177/1464420720928378.

[34] Z. Rahimi, W. Sumelka, and S. Shafiei. The analysis of non-linear free vibration of fgm nanobeams based on the conformable fractional non-local model. *Bulletin of the Polish Academy of Sciences Technical Sciences*, 66(No 5):737–745, 2018. doi: 10.24425/bpas.2018.125341.

[35] D.Q. Chan, T.Q. Quan, B.G. Phi, D. Van Hieu, and N.D. Duc. Buckling analysis and dynamic response of fgm sandwich cylindrical panels in thermal environments using nonlocal strain gradient theory. *Acta Mechanica*, 233(6):2213–2235, 2022. doi: 10.1007/s00707-022-03212-8.

[36] P. Stempin and W. Sumelka. Formulation and experimental validation of space-fractional timoshenko beam model with functionally graded materials effects. *Computational Mechanics*, 68(3):697–708, 2021. doi: 10.1007/s00466-021-01987-6.

[37] A. M. Zenkour and A. F. Radwan. Bending and buckling analysis of fgm plates resting on elastic foundations in hygrothermal environment. *Archives of Civil and Mechanical Engineering*, 20(4):112, 2020. doi: 10.1007/s43452-020-00116-z.

[38] B. Niesterowicz, P. Dunaj, and S. Berczyński. Timoshenko beam model for vibration analysis of composite steel-polymer concrete box beams. *Journal of Theoretical and Applied Mechanics*, 58(3):799–810, 2020. doi: 10.15632/jtam-pl/122389.

[39] A. Saimi, I. Bensaid, and I.E. Houalef. Dynamic analysis of a porous microbeam model based on refined beam strain gradient theory via differential quadrature hierarchical finite element method. *Advances in Materials Research*, 12(2):133–159, 2023. doi: 10.12989/amr.2023.12.2.133.

[40] A. Karamanli and M. Aydogdu. Structural dynamics and stability analysis of 2d-fg microbeams with two-directional porosity distribution and variable material length scale parameter. *Mechanics Based Design of Structures and Machines*, 48(2):164–191, 2020. doi: 10.1080/15397734.2019.1627219.

[41] J.L. Mantari and C. Guedes Soares. Four-unknown quasi-3d shear deformation theory for advanced composite plates. *Composite Structures*, 109:231–239, 2014. doi: 10.1016/j.compstruct.2013.10.047.

[42] Y. Xing and B. Liu. High-accuracy differential quadrature finite element method and its application to free vibrations of thin plate with curvilinear domain. *International Journal for Numerical Methods in Engineering*, 80(13):1718–1742, 2009. doi: 10.1002/nme.2685.